# **Evolution of Force Chains Explains the Onset of Strain Stiffening in Fiber Networks**

Mainak Sarkar, Jacob Notbohm

Department of Engineering Physics, University of Wisconsin-Madison, Madison, WI, USA

### **Abstract**

Fiber networks are the primary structural components of many biological structures, including the cell cytoskeleton and the extracellular matrix. These materials exhibit global nonlinearities, such as stiffening in extension and shear, during which the fibers bend and align with the direction of applied loading. Precise details of deformations at the scale of the fibers during strain stiffening are still lacking, however, as prior work has studied fiber alignment primarily from a qualitative perspective, which leaves incomplete the understanding of how the local microstructural evolution leads to the global mechanical behavior. To fill in this gap, we studied how axial forces are transmitted inside the fiber network along paths called force chains, which continuously evolve during the course of deformation. We performed numerical simulations on two-dimensional networks of random fibers under uniaxial extension and shear, modeling the fibers using beam elements in finite element software. To quantify the force chains, we identified all chains of connected fibers for which the axial force was larger than a preset threshold and computed the total length of all such chains. To study the evolution of force chains during loading, we computed the derivative of the total length of all force chains with respect to the applied engineering strain. Results showed that the highest rate of evolution of force chains coincided with the global critical strain for strain stiffening of the fiber network. Therefore, force chains are an important factor connecting understanding of the local kinematics and force transmission to the macroscale stiffness of the fiber network.

## Introduction

Fiber networks are the primary structural components of biological structures like the cellular cytoskeleton [1–3], blood clots [4] and the extracellular matrix within tissues [5]. These networks exhibit heterogeneities in stiffness at the length scale of the fibers [6–9], which renders the deformation field to be nonaffine [10–18], meaning that deformations at the scale of the fibers differ considerably from deformations at the scale of the global network. Fibers constituting these networks are slender and soft in bending, and their local deformations are dominated by bending modes [19–21]. Globally, these networks exhibit strain stiffening in both uniaxial extension and shear, causing the stress–strain curve to bend upward in the shape of the letter J [22–27] (e.g., Fig. 1). This global nonlinearity is primarily attributed to realignment of fibers along the direction of loading by means of fiber bending rather than inherent nonlinearity of the individual fibers. Several attempts were made to describe strain stiffening by characterizing the local fiber deformations in terms of excess lengths, defined as the difference between the fiber's full length and its end-to-end distance [19, 20, 28]. However, as we will show, the excess length of a fiber depends not only on the load applied but also on the alignment of the fiber with respect to the loading direction, which causes wide variation in excess lengths, meaning that such characterization does not provide a robust connection between the evolution of the local microstructure and the mechanical behavior of the global network.

Despite the fact that deformations of the network are governed by fiber bending, strain stiffening of the network is initially caused not by fiber bending but rather by axial forces in the fibers. Axial forces in always exist in the fibers to satisfy force equilibrium at the nodes [29]. Bending of fibers passively induces axial forces in neighboring fibers; these axial forces transmit from one fiber to the next along

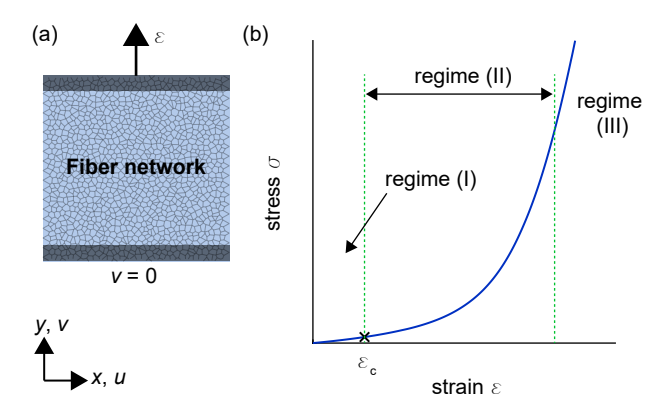


Figure 1: Global strain stiffening in fiber networks. (a) Schematic of a fiber network subjected to uniaxial extension. (b) Common J-shaped stress–strain curve indicating three distinct regimes, which are typical in the deformation of fiber networks. The linear regime I culminates at a critical strain ( $\varepsilon_c$ , labeled with the "×" symbol), where the nonlinear regime II begins. Regime III is again linear and occurs at large strains. The present study focuses on regimes I and II.

preferred routes, often referred to as force chains [29–33]. The concept of force chains is derived from the physics of granular media, wherein grain-to-grain contacts transmit forces [34, 35], leading to chains of force transmission that can explain global mechanical behaviors like the development of shear strength [36, 37]. Given that fiber networks are analogous to granular media in that both have a bi-modulus response to tension and compression [32, 38], a rigorous quantification of force chains in fiber networks may establish a precise connection between the local mechanics and the global nonlinearity. In fiber networks, the force chains form and continuously grow as the deformation progresses. A few studies, *e.g.*, refs. [32, 33], studied the structural features of force chains in fiber networks and their dependence on fiber properties and connectivity, but a systematic quantification of their evolution with the deformation of network is still lacking.

Here, we studied force transmission across fiber networks by quantifying the evolution of force chains and mapping it to the global strain stiffening. We used two-dimensional (2D) numerical models of fiber networks resembling the structure of type I collagen gels and applied displacement boundary conditions to the models using finite element (FE) software to solve for the deformed states. We began our study by quantifying excess lengths and demonstrating how excess lengths are insufficient to connect the local fiber morphology and deformation to the global mechanical behavior of the network. We then turned to force chains, using an algorithm to identify and quantify the force chains in the deformed fiber network. The total lengths of all force chains and its first-order derivative with respect to the global engineering strain were recorded during the course of deformation. The results showed that the highest rate of evolution of force chains coincided with the onset of strain stiffening of the fiber network. Thus, force chains are an important factor connecting local kinematics and microscale force transmission to the macroscale behavior of the fiber network.

## **Methods**

#### **Network Generation**

We employed simplified 2D models to study force transmission in biopolymer fiber networks like those of type I collagen. Prior studies showed that the 2D network models exactly capture an observation of non-linear stiffening of three-dimensional collagen gels, namely that the tangent modulus is linearly proportional to the applied stress [19]. Further, noting that the collagen networks are intrinsically sub-isostatic [39, 40]

meaning that their nodal coordination number (z) is below Maxwell's isostatic threshold of 2d (with d being the dimension of the system) [41], we generated similar sub-isostatic 2D Voronoi and lattice-based random fiber networks with average connectivity z = 3, which is below Maxwell's 2D isostatic threshold of 4.

As the models based on a Voronoi network resemble type I collagen more closely [42, 43], they were used for the majority of this study. Generation of Voronoi networks followed the method described in refs. [40, 44]. In brief, random seeds were used in a 2D domain to generate a Voronoi tessellation. Fibers were deposited along the edges of resulting polygons to generate the network, similar to the schematic representation shown in Fig. 2a. As the fiber lengths in Voronoi networks are Poisson-distributed [45], they can be fully characterized by the mean fiber length  $L_{\rm f}$ . Where stated in the "Results" section, we also explored force transmission on a 2D irregular hexagonal lattice-based network (Fig. 2b). Such networks are qualitatively similar to certain types of collagen networks found in the lung tissues [46, 47]. This irregular network was generated through random perturbations of the position of every node on a regular hexagonal lattice (method similar to ref. [48]). The size of the network models were always  $\geq 25L_{\rm f}$ , which was considered to be large enough that the models were free of size effects, following the recommendations of ref. [8].

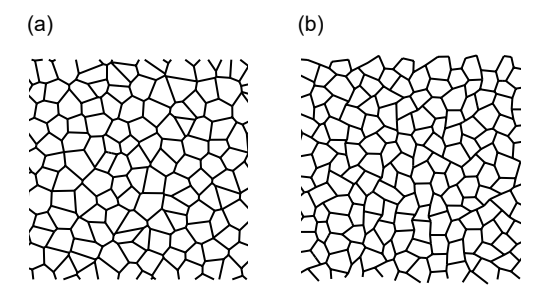


Figure 2: Geometries used to model fiber networks. (a) A portion of the Voronoi network of random fibers. (b) A portion of the random irregular hexagonal lattice-based network. Both models have average nodal coordination number z = 3.

#### **Fiber Mechanical Properties**

Similar to prior work [8, 49–51], we modeled the fibers as linear, elastic Timoshenko beams having bending stiffness  $k_b$ , axial stiffness  $k_a$  and shearing stiffness  $k_s$ . The most important quantity is the ratio of bending stiffness to axial stiffness, often referred to as the dimensionless bending stiffness,  $\kappa = k_b/k_a = (E_f I_f)/(E_f A_f L_f^2)$ , where  $E_f$ ,  $A_f$  and  $I_f$  are the Young's modulus, cross-sectional area, and moment of inertia of each fiber [29, 49, 52, 53]. In this study, we used a value of  $\kappa = 1 \times 10^{-4}$ , which is a typical value for fibers in type I collagen networks [19, 20, 54, 55]. We kept the ratio of shearing stiffness to axial stiffness of each fiber,  $k_s/k_a$ , constant at 1/2.

## **Finite Element Simulations**

Different displacement boundary conditions were imposed on the fiber networks by performing 2D FE simulations using the commercially available FE software Abaqus (Dassault Systèmes). Each fiber was modeled using two three-noded quadratic beam elements, and connections between fibers were "welded" such that they transmitted both forces and moments. The implicit dynamic quasistatic solver with the nonlinear geometry option was used, as in our prior work [56, 57]. To ensure that the solver converged to static equilibrium amidst strong geometric nonlinearities prevalent in the system, we applied the displacement boundary condition in small load steps following the recommendations of ref. [58]. The use of 0.05% global strain at each load step eliminated the convergence bias for all practical purposes.

The global stress and strain measures reported in this study are the engineering stress and strain. The engineering stress, quantified following the method in ref. [59], was computed by taking the sum of the reaction forces in the loading direction at nodes subjected to boundary displacements and dividing by the initial cross-sectional area.

#### **Analysis of Force Chains**

The data generated in the FE simulations were post-processed to analyze the force chains in the deformed configurations of the network. We wrote an algorithm (similar to refs. [32, 60]) to quantify the force chains at each deformed state, as described in the following three steps.

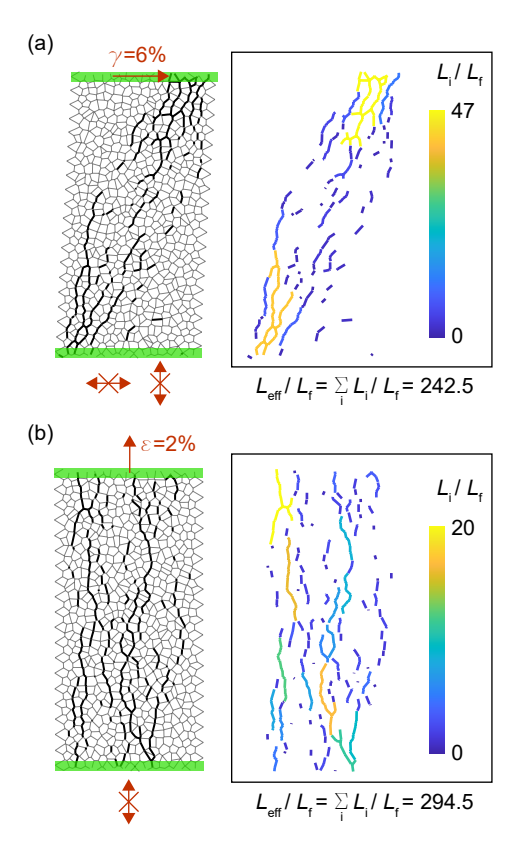


Figure 3: Analysis of force chains. (a, b) Identification of fibers constituting force chains in networks subjected to shear  $\gamma$  (a) or extension  $\varepsilon$  (b). The bold black lines inside the network denote the fibers above the chosen axial stress threshold and constitute force chains. The individual force chains were then isolated (shown in the boxes on the right) and their lengths ( $L_i$ ) were calculated. Finally, lengths of all the force chains were added to compute the parameter  $L_{\rm eff}$ . The values of  $L_{\rm eff}$  were normalized by the fiber length ( $L_f$ ).

### Step 1: Identification of fibers constituting force chains

We began by choosing a threshold for axial strain in the fibers. The threshold was chosen similarly to ref. [32] and was the axial strain of the most stressed fiber at a chosen value of global normal strain. Precise values of the global normal strain and threshold are described in the "Results" section. The algorithm identified the subset of fibers with axial strains larger than the threshold. This subset of fibers constituted the force chains, which was retained for the next steps of analysis.

#### Step 2: Detection of individual force chains

The next step was to identify individual force chains. The algorithm worked only on the subset of fibers from Step 1 and searched for the neighboring fibers of a given fiber to detect continuous chains of fibers experiencing axial strain above the threshold. The detected force chains sometimes contained several branches.

### Step 3: Quantification of force chains

The lengths of the individual force chains  $(L_i)$  were determined (see Fig. 3). The lengths of all of the force chains were added to obtain the parameter  $L_{\text{eff}} = \sum_i L_i$ , which is defined as the effective length of all force chains occurring within the network under the load step of interest.

#### **Evolution of Force Chains**

With the force chain parameter  $L_{\rm eff}$  defined at every load step, the evolution of  $L_{\rm eff}$  with applied engineering strain was obtained. We computed the rate of evolution of force chains by taking the derivative of  $L_{\rm eff}$  with respect to the applied engineering strain, i.e.,  $dL_{\rm eff}/d\varepsilon$  in tension and  $dL_{\rm eff}/d\gamma$  in shear. The derivative at a given point was calculated by fitting a line to five points across the point of interest.

## **Results and Discussion**

## **Strain Stiffening and Excess Lengths**

The schematic stress-strain response of a typical sub-isostatic fiber network (Fig. 1) depicts three distinct regimes: regime I is linear with a small amount of fiber bending, regime II is nonlinear with a large amount of fiber bending, and regime III corresponds to stretching of the fibers [59]. Here we focus on regimes I and II, wherein the fibers predominantly undergo bending-dominated deformations. The global strain at the onset of regime II, *i.e.*, at the onset of nonlinear stiffening, is called the critical strain (represented by  $\varepsilon_c$  in Fig. 1b). As a fiber bends, its excess length (the difference between contour length and node-to-node distance) increases [61]. To investigate if excess lengths of the fibers are representative of the localized deformation of fibers, we quantified the excess length  $\xi$  of all fibers in a network subjected to an intermediate uniaxial extension of 10% engineering strain (Fig. 4a, b). The fibers that were aligned with the loading axis (angle to loading axis  $\theta \leq 35^{\circ}$ ) exhibited excess lengths  $\xi$  close to zero (Fig. 4c). On the contrary, values of  $\xi$  were large for fibers at larger angles ( $\theta > 35^{\circ}$ ) to the loading axis. Thus, at a given applied global strain, excess lengths depend at least in part on initial fiber alignment, and the range of excess lengths of fibers can be large, indicating that quantification of excess lengths of fibers alone is not sufficient to understand the microstructural evolution of fiber networks.

## Force Transmission in Fiber Networks

#### Network geometry

We studied force transmission in a 2D Voronoi fiber network having domain width  $25L_{\rm f}$  and height  $50L_{\rm f}$  (Fig. 5a). This domain size was large enough for the network to be free of size effects (following ref. [8]), and the rectangular shape, with a height-to-width ratio of 2, was chosen to minimize boundary effects.

#### Uniaxial extension

The first boundary condition studied was uniaxial extension, wherein a subset of nodes at the bottom of the network was fixed and a subset of nodes at the top was translated in the positive y direction. The

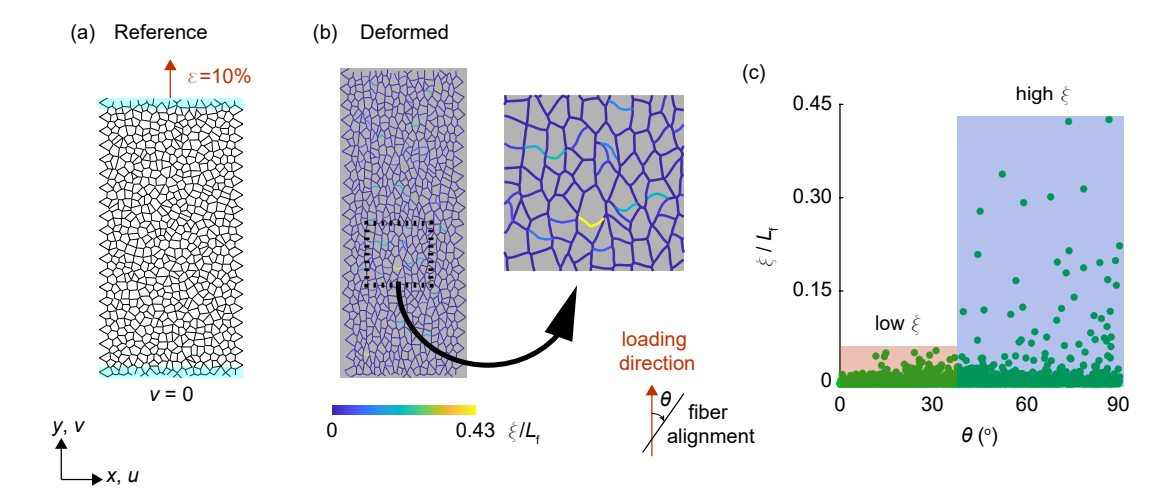
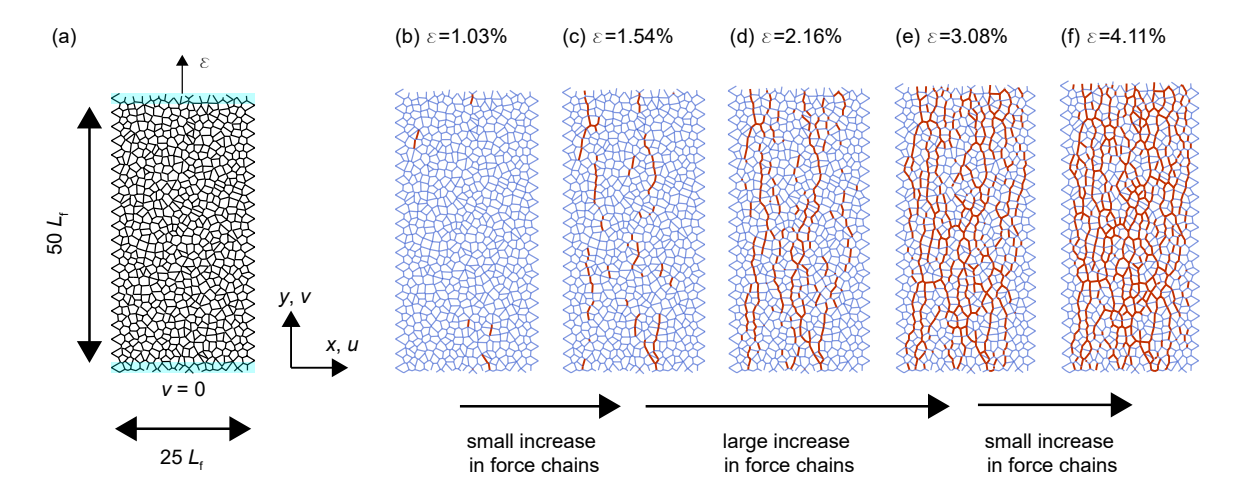


Figure 4: Quantification of excess lengths of fibers in a deformed network. (a) Reference configuration of a fiber network subjected to uniaxial extensile strain  $\varepsilon = 10\%$ . (b) Deformed configuration of the network. The deformed fibers are color coded based on the values of their excess lengths ( $\xi$ ) normalized by the average fiber length ( $L_f$ ). A small portion of this network is magnified to show the varying magnitudes of excess lengths prevalent in the fibers. (c) Normalized excess length for each fiber is plotted against its alignment  $\theta$  with the loading direction in the deformed configuration of the network. While  $\xi$  is small for fibers closely aligned to the loading axis ( $\theta < 35^{\circ}$ ), large values of  $\xi$  are observed for non-aligned fibers.

regions where nodes were fixed or translated are shaded blue in Fig. 5a. As described in the "Methods" section, translation was applied in small load steps, with 0.05% strain per step. We identified force chains in the network at each load step. At each configuration, the fibers constituting force chains experienced axial strains more than a threshold,  $2.13 \times 10^{-4}$ , which was chosen to filter out the most stressed fiber at 0.5% global normal strain. The same threshold axial strain was used for identifying force chains when this network was subjected to shear described later. Some representative deformed configurations are shown in Fig. 5b–f with the force chains highlighted red. Qualitatively, there appears to be a small increase in the number of force chains from  $\varepsilon = 1.03\%$  to 1.54% (Fig. 5b–c), a large increase from  $\varepsilon = 1.54\%$  to 3.08% (Fig. 5c–e), and then again a small increase from  $\varepsilon = 3.08\%$  to 4.11% (Fig. 5e–f).

The stress-strain response was recorded as deformation progressed (Fig. 6a, b), and at each current configuration of this network, the sum of the length of all force chains  $L_{\rm eff}$  was calculated and normalized by the average fiber length  $L_{\rm f}$ . The dimensionless force chain parameter increased monotonically with the applied strain  $\varepsilon$  until it reached an asymptotic limit, which in the present case was  $\approx 10^3$ , which corresponded to  $\approx 53\%$  of all fibers within the network (Fig. 6c). Recalling the uneven increase in the number of force chains with applied  $\varepsilon$  observed qualitatively in Fig. 5b–f, we wanted to explore the rate of growth of the force chains by taking the first-order derivative of  $L_{\rm eff}$  with respect to the applied global strain  $\varepsilon$ ,  $dL_{\rm eff}/d\varepsilon$ . This rate, normalized by the average fiber length  $L_{\rm f}$ , monotonically increased at small strains until it reached a peak at  $\varepsilon = 2.16\%$ , followed by a decrease as strain increased further (Fig. 6d). Interestingly, the value of strain corresponding to the highest rate of increase of force chains ( $\varepsilon = 2.16\%$ , labeled "×" in Fig. 6d) separated regime I from regime II on the stress-strain curve in Fig. 6b. Therefore, the highest rate of evolution of force chains coincided with the onset of strain stiffening.

Next, we quantitatively verified that the maximal rate of increase in force chains corresponded to the onset of strain stiffening. We fit the global tangent modulus E to the stress  $\sigma$  according to  $E \sim \sigma^{\alpha}$ , where  $\alpha$  is a fitting factor called the stiffening exponent. Fitting data in the linear regime I gave  $\alpha \approx 0$ , and in regime II, it gave  $\alpha \approx 1$  (see Fig. 7a). These values of  $\alpha$  match the values reported in prior modeling and experiments in gels of collagen fibers [19, 59]. Given that the transition from  $\alpha \approx 0$  to  $\alpha \approx 1$  occurs



**Figure 5:** Identification of force chains in a fiber network under uniaxial extension. (a) A representative rectangular Voronoi network was subjected to uniaxial extension. The nodes at the bottom of the network were fixed, and the nodes at the top of the network were subjected to quasistatic, uniform, uniaxial extension  $\varepsilon$ . (b–f) Force chains were identified and shown as bold red lines on the deformed networks at several global normal strains  $\varepsilon$ . Qualitatively, there appears to be a small increase in the number of force chains from b to c (i.e., from  $\varepsilon = 1.03\%$  to 1.54%) and e–f (i.e., from  $\varepsilon = 3.08\%$  to 4.11%). A large increase in the number of force chains is observed from c to e (i.e., from  $\varepsilon = 1.54\%$  to 3.08%).

gradually, the transition from regimes I to II is also gradual, meaning there is no clear, distinct point at which to define the onset of regime II. With this in mind, we ensured that the force chain-based prediction of the onset of strain stiffening in Fig. 6d gives a reasonable representation of this transition. To this end, we verified that the strain corresponding to the maximal rate of growth of force chains was robust to the chosen value of threshold strain used to define the force chains. Recall that the threshold strain used in Fig. 6 was  $2.13 \times 10^{-4}$ , which happened to be the axial strain in the most stressed fiber at  $\varepsilon = 0.5\%$ . Using this threshold, the predicted onset of stiffening corresponded to  $\alpha = 0.33$  (marked "×" in Fig. 7a). We repeated the analysis for different thresholds. A smaller threshold,  $1.05 \times 10^{-4}$  (corresponding to the axial strain in most stressed fiber at  $\varepsilon = 0.25\%$ ) predicted the onset of stiffening at  $\alpha = 0.17$  (marked " $\square$ " in Fig. 7a). A slightly larger threshold,  $3.27 \times 10^{-4}$  (corresponding to the axial strain in most stressed fiber at  $\varepsilon = 0.75\%$ ) predicted the onset of stiffening at  $\alpha = 0.46$  (marked ">" in Fig. 7a). The stiffening exponents ( $\alpha$ ) of 0.17 and 0.46 can be thought of as lower and upper bounds describing the gradual transition between regimes I and II, and therefore the choice of our threshold  $(2.13 \times 10^{-4})$  that predicted stiffening at  $\alpha = 0.33$  was reasonable. The predictions of the onset of stiffening were marked on a logarithmic plot of global tangent modulus (E) vs. strain (E) as well (Fig. 7b), as this representation is common in the literature (e.g., refs.[20, 48]).

To ensure that the ability of force chains in estimating the onset of strain stiffening is not a characteristic of only 2D Voronoi networks, we studied force chains on a 2D lattice network of similar characteristics (Fig. 10, Appendix A). Again we observed that the highest rate of evolution of force chains coincided with the onset of strain stiffening at 3.4% strain with a stiffening exponent  $\alpha \approx 0.4$ . Additionally, considering that fiber networks are subject to size effects wherein network size and boundary conditions can affect the mechanics [8, 51, 62], we verified that force chains also describe the onset of stiffening in a network with square geometry, designed to amplify the boundary effect (Appendix B and Fig. 11).

Simple shear combined with uniaxial tensile prestress

The presence of residual stress or prestress is common in biopolymer networks [63–66]. Several studies (e.g., refs. [20, 48]) reported the shearing stress–strain response of 2D fiber networks subjected to shearing

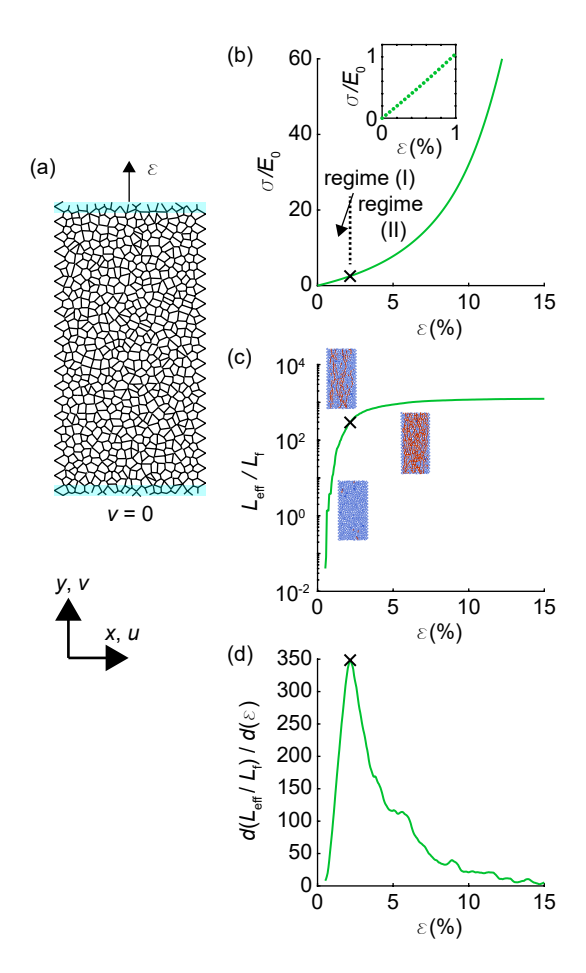


Figure 6: Quantification of force chains in a fiber network under uniaxial extension. (a) The Voronoi network (same dimensions as Fig. 5) was subjected to uniaxial extension. The nodes at the bottom of the network were fixed, and the nodes at the top of the network were subjected to quasistatic, uniform, uniaxial extension  $\varepsilon$ . (b) Stress–strain  $(\sigma - \varepsilon)$  curve. The stress axis was normalized by the small strain modulus  $(E_0)$ . The inset shows the stress response at small  $\varepsilon \in [0, 1\%]$ . (c) Evolution of the total length of force chains  $(L_{\text{eff}})$  with  $\varepsilon$ . Insets show schematic diagrams of deformed networks with force chains shown in red. The force chain parameter  $L_{\text{eff}}$  was normalized by the average fiber length  $(L_f)$ . (d) The rate of evolution of force chains,  $dL_{\text{eff}}/d\varepsilon$  plotted against the applied global strain  $\varepsilon$ . The rate was normalized by the average fiber length  $(L_f)$ . The peak rate observed at  $\varepsilon = 2.16\%$  (marked by "×") corresponds to the onset of strain stiffening and separates regimes I and II in the  $\sigma - \varepsilon$  curve in panel b. The symbol "×" corresponds to the same strain in panels b and c.

with a uniaxial tensile prestress. Uniaxial tensile prestress decreases the critical shear strain and increases the small strain shear modulus of network. Here we questioned if the quantification of force chains can predict these global behaviors.

In our model, prestress was induced in an undeformed network by subjecting it to uniaxial extension  $\varepsilon$  and considering this prestressed configuration as the starting point, from which simple shear  $\gamma$  was applied in small steps (0.05% shear/step). Application of boundary conditions was done as follows. Displacement boundary conditions were imposed on the nodes at the bottom and the top of the network (highlighted blue in Fig. 8a). The subset of nodes at the bottom of network was fixed. The subset of nodes at the top of network was translated in the positive y direction during pretension and, subsequently, the positive x direction during shear (see Fig. 8a and 9a). We identified the fibers constituting force chains at each load step during shear. The axial strain threshold in fibers used for the identification of force chains was  $2.13 \times 10^{-4}$ , which was the same value considered during the study of uniaxial extension on this network as

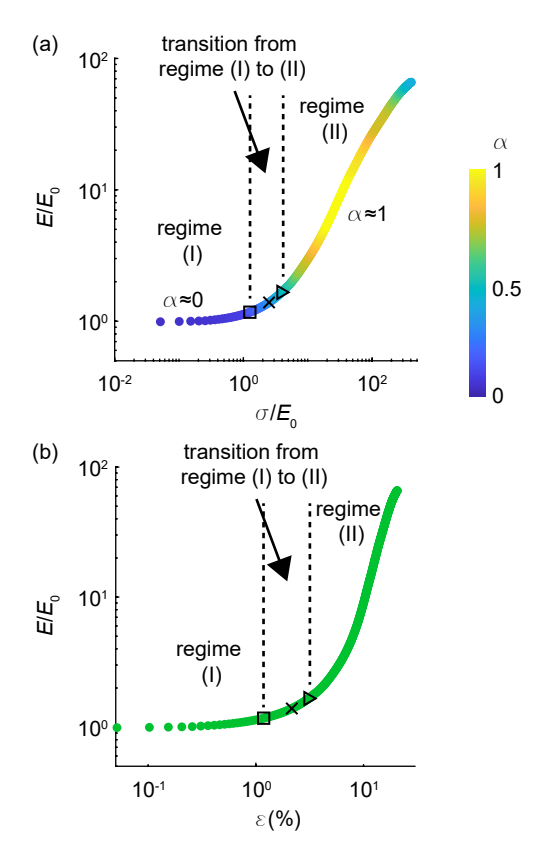


Figure 7: Robustness of the chosen threshold axial strain used in identifying force chains for the prediction of the onset of strain stiffening. (a) Tangent modulus (*E*) as a function of stress  $\sigma$  on the network under uniaxial extension described in Fig. 6. Both axes were normalized by the small strain modulus  $E_0$ . Tangent modulus is independent of stress in the linear regime I ( $\alpha \approx 0$ ) and approximately proportional to stress in nonlinear regime II ( $\alpha \approx 1$ ). Stiffening is observed at the point marked by "×" ( $\alpha = 0.33$ ), which was based on force chains defined by a threshold of  $2.13 \times 10^{-4}$ . Altering this threshold to  $1.05 \times 10^{-4}$  or  $3.27 \times 10^{-4}$  changed the prediction of the onset of strain stiffening to the locations marked " $\square$ " ( $\alpha = 0.17$ ) and ">" ( $\alpha = 0.46$ ), respectively. All predictions fall within the zone of gradual transition from regimes I to II. (b) Tangent modulus (*E*) as a function of applied strain  $\varepsilon$ . The tangent modulus was normalized by small strain modulus  $E_0$ . As in panel a, the corresponding points of the onset of stiffening for the three different thresholds are labeled.

described earlier. Representative current configurations in shear with force chains are shown in Fig. 8b–f. Here we again noticed the uneven increase in the number of force chains as deformation progressed (similar to Fig. 5).

Shear stress–strain  $(\tau - \gamma)$  responses of the network were "J-shaped" for all three levels of pretension used,  $\varepsilon = 0\%$ , 0.5% and 1% (Fig. 9b). At a given value of pretension, force chains (quantified by  $L_{\rm eff}$ ) evolved monotonically with shear strain  $\gamma$  until saturation (Fig. 9c), and the rate of evolution of force chains  $(dL_{\rm eff}/d\gamma)$  consistently attained a peak at the onset of strain stiffening (marked "×" in Fig. 9d) which separated regimes I and II in the stress–strain ( $\tau$ – $\gamma$ , Fig. 9b) and modulus–strain (G– $\gamma$ , Fig. 9e) curves. The recorded values of shear strain at the onset of stiffening were 6.69%, 6.17% and 5.14% for pretension 0%, 0.5% and 1%, respectively. The reduction in the magnitude of strain at the onset of stiffening with increasing pretension was consistent with previously reported trends in prestressed networks [20, 48]. The predicted points of onset of shear stiffening corresponded to stiffening exponents  $\approx$  0.3–0.4 depicting the transition between regimes I ( $\alpha \approx 0$ ) and II ( $\alpha \approx 1$ ) (Fig. 9f).

Another noteworthy phenomenon was that the tangent shear modulus (G) of the network at small shear  $(e.g., \text{ at } \gamma \le 2\%)$  increased with applied pretension (Fig. 9e and inset in Fig. 9b), as has been reported

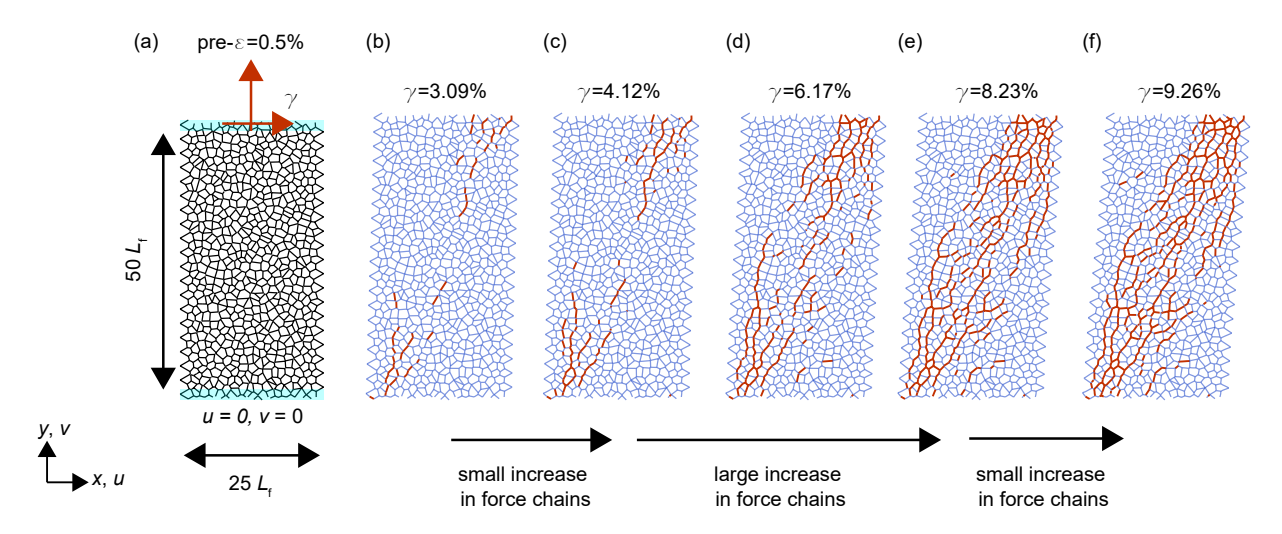


Figure 8: Identification of force chains in a prestressed fiber network under shear. (a) The network was prestressed in uniaxial extension  $\varepsilon = 0.5\%$  and then subjected to shear  $\gamma$ . The nodes at the bottom of the network were fixed, and the nodes at the top of the network were displaced first in the positive y direction and then in the positive x direction. (b–f) Force chains were identified and shown as bold red lines on the deformed networks at several global shear strains  $\gamma$ . We observe a small increase in the number of force chains from b to c (i.e., from  $\gamma = 3.09\%$  to 4.12%) and e–f (i.e., from  $\gamma = 8.23\%$  to 9.26%). A large increase in the number of force chains is observed from c to e (i.e., from  $\gamma = 4.12\%$  to 8.23%).

previously [20]. To investigate if the total length of force chains ( $L_{\rm eff}$ ) could explain this, we calculated  $L_{\rm eff}$  at  $\gamma=2\%$  for different values of prestress  $\varepsilon$ . It was interesting to note that the tangent shear moduli at 2% shear ( $G_{\rm T,\varepsilon}$ ) were positively correlated to the normalized total length of force chains (Fig. 9g), meaning that the force chains could explain the increase in the small strain modulus with prestress.

To verify that these findings under pretension and shear were consistent for fiber networks of different size, these simulations were repeated for a square fiber network. Results were consistent, with force chains describing the onset of stiffening and corresponding to the small strain shear modulus (Appendix B and Fig. 12).

# **Conclusions**

To better understand how the localized deformation of fibers within a network leads to global stiffening, we studied how forces are transmitted across the fiber network. We quantified the evolution of force chains in simulated 2D fiber network models subjected to extension and shear. Results indicated that the rate of growth of force chains predicted the transition from linear to strain stiffening material behavior. In the initial linear regime I, the growth of force chains accelerated, and the highest rate of growth corresponded with the onset of the nonlinear strain stiffening regime II. This stiffening continued amidst a decelerating growth and subsequent saturation of the number of force chains. These findings were consistent for different boundary conditions (uniaxial tension, simple shear, and shear combined with pretension) and for different network architectures and geometries. Therefore, the analysis of force chains in fiber networks offers a reasonable quantitative means to define the global critical strain at the onset of strain stiffening. This study further highlights the key role that the axial forces in fibers play in causing the nonlinear stiffening, irrespective of their bending mode of deformation. Our findings on the importance of the rate of evolution of force chains may be useful in studies of cell–matrix interactions, for example, by determining how force chains within the extracellular matrix in the vicinity of a cell affect cell sensing and response to the surrounding environment [32]. Our results could also aid in a more systematic understanding of the role of local fiber morphology

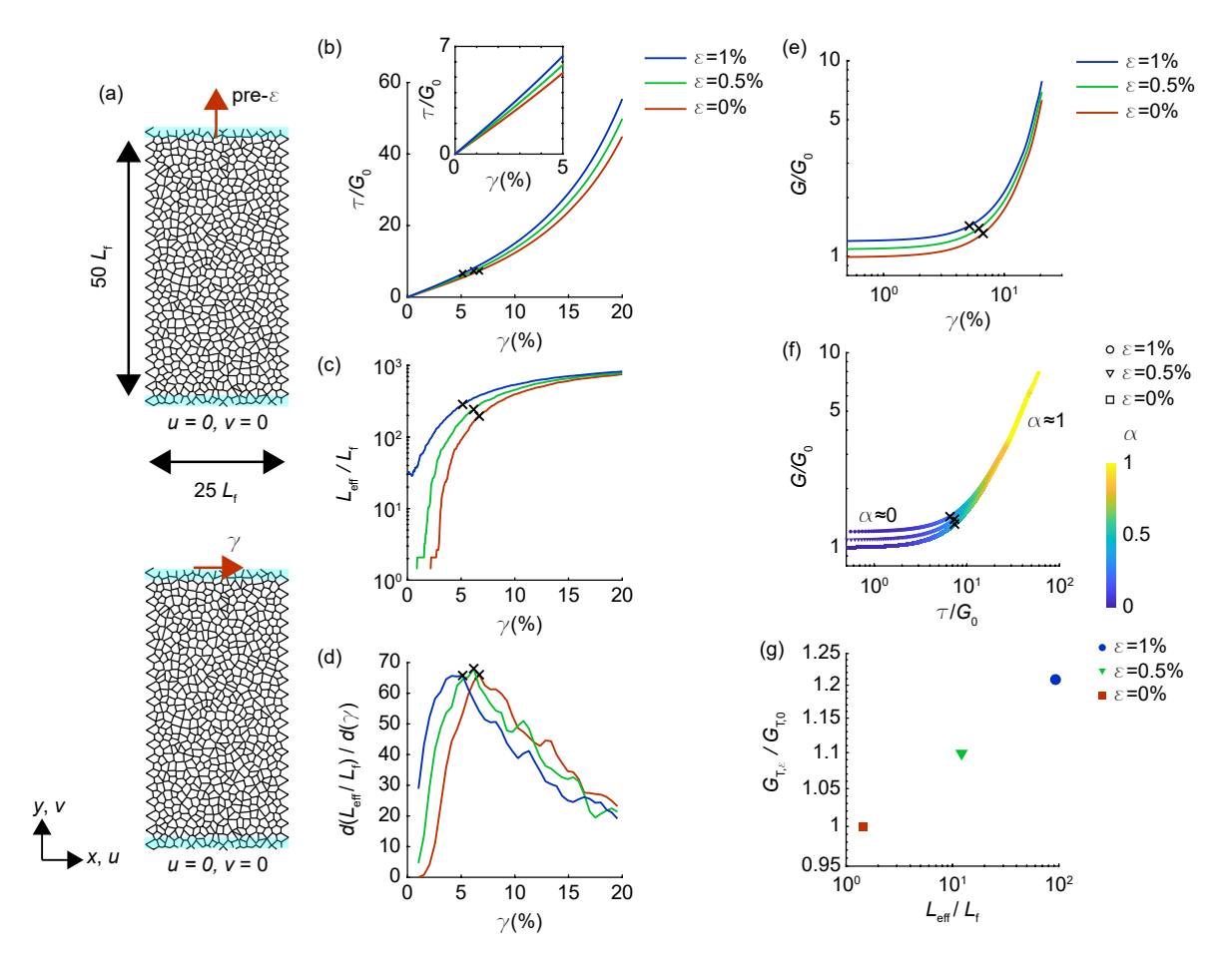


Figure 9: Quantification of force chains in prestressed network under shear. (a) The prestressed network was subjected to shear. The nodes at the bottom of the network were fixed, and the nodes at the top of the network were displaced to induce uniaxial pretension  $(\varepsilon)$  followed by shear  $(\gamma)$ . (b) Shear stress-strain  $(\tau-\gamma)$  responses of the network at pretension  $\varepsilon=0\%$ , 0.5% and 1%. The inset shows the stress responses at small shear strain,  $\gamma\in[0,5\%]$ . The stress axis was normalized by the small strain shear modulus of the network at zero prestress  $G_0$ . (c) Evolution of force chains  $(L_{\rm eff})$  with shear  $\gamma$  at pretension  $\varepsilon=0\%$ , 0.5% and 1%. (d) Normalized rate of evolution of force chains  $(d(L_{\rm eff}/L_f)/d\gamma)$  with shear at pretension  $\varepsilon=0\%$ , 0.5% and 1%. The peak rates (marked "×") correspond to the onset of strain stiffening. The quantities in the  $\gamma$  axis of panels  $\gamma$  and 1 were normalized by fiber length  $\gamma$  (e) Tangent shear modulus  $\gamma$  as a function of  $\gamma$ . (f) Tangent shear modulus  $\gamma$  as a function of stress  $\gamma$  showing regime I having  $\gamma$  and  $\gamma$  are 1 having  $\gamma$  and 1 having  $\gamma$  are 1 having  $\gamma$  and 1 having  $\gamma$  are 1 having  $\gamma$  and 1 having  $\gamma$  are 1 having  $\gamma$  and 1 ha

and connectivity in the design of synthetic fibrous hydrogels with tunable critical strain [67, 68].

# **Conflicts of Interest**

There are no conflicts to declare.

# Acknowledgments

We thank R. Lakes and R. Thevamaran for useful discussion.

# **Funding Data**

This work was supported by the National Science Foundation grant number CMMI-1749400.

# Appendix A

Appendix A contains Fig. 10.

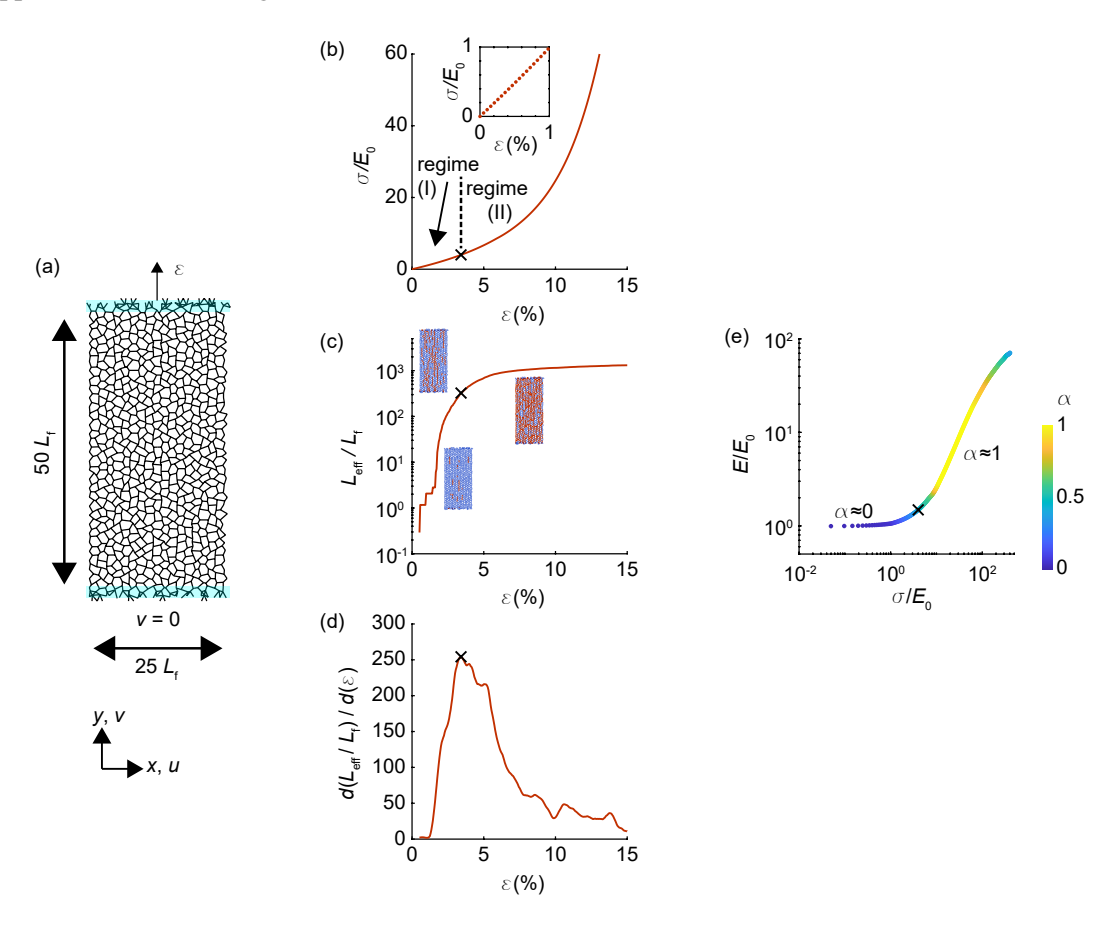


Figure 10: Quantification of force chains in an irregular lattice network under uniaxial extension. (a) The lattice-based network of rectangular domain (height/width = 2) was subjected to uniaxial extension. The nodes at the bottom of the network were fixed, and the nodes at the top of the network were subjected to uniform uniaxial extension  $\varepsilon$ . (b) Stress-strain ( $\sigma$ - $\varepsilon$ ) curve. The stress axis was normalized by the small strain modulus ( $E_0$ ). The inset shows the stress response at small strain,  $\varepsilon \in [0, 1\%]$ . (c) Evolution of the total length of force chains ( $L_{\rm eff}$ ) with  $\varepsilon$ . Insets show schematic diagrams of deformed networks with force chains shown in red. The force chain parameter  $L_{\rm eff}$  was normalized by the fiber length ( $L_{\rm f}$ ). (d) Rate of evolution of force chains,  $dL_{\rm eff}/d\varepsilon$  plotted against the applied global strain  $\varepsilon$ . The rate was normalized by the fiber length ( $L_{\rm f}$ ). The peak rate observed at  $\varepsilon = 3.4\%$  (marked by "×") corresponds to the onset of strain stiffening and separates regimes I and II in the  $\sigma$ - $\varepsilon$  curve in panel b. The symbol "×" corresponds to the same strain in panels b, c, and d. (e) Tangent modulus (E) as a function of global stress  $\sigma$  showing regimes I and II having exponents  $\alpha \approx 0$  and  $\alpha \approx 1$ , respectively. The axes were normalized by the small strain modulus  $E_0$ . The highest rate of evolution of force chains corresponds to a stiffening exponent  $\alpha \approx 0.4$  (marked "×").

# **Appendix B: Prediction of Global Mechanics Amidst Boundary Effects**

Proximity of a boundary can affect the mechanical response of sub-isostatic fiber networks [8, 51, 62]. Here we investigated if the force chain-based prediction of the onset of strain stiffening described so far also occurs amidst an amplified boundary effect. For this study, we increased the effect of boundaries by

reducing the ratio of height to width (h/w) of the network to 1 (square domain, Fig. 11a) from the prior value of 2. In uniaxial tension, this change in aspect ratio resulted in a modest change in small strain modulus ( $\approx 10\%$  increase, Fig. 11b) and a larger change in the incremental Poisson's ratio ( $\approx 33\%$  increase, Fig. 11c), where the incremental Poisson's ratio  $v_i$  was calculated following ref. [69] according to

$$v_{\rm i} = -rac{d[\ln(1+arepsilon_{
m l})]}{d[\ln(1+arepsilon)]},$$

where  $\varepsilon$  and  $\varepsilon_1$  are the strains in the loading and transverse directions respectively. These effects were consistent with prior observations [8, 51, 70]. With the boundary effect established, we next applied uniaxial tension and studied the force chains (Fig. 11d–f). As with prior observations, the highest rate of evolution of force chains predicted the onset of strain stiffening, at a normal strain of 1.71% and a stiffening exponent  $\alpha = 0.24$  (Fig. 11g).

Boundary effects were also studied in shear (Fig. 12a), and it was interesting to observe a pronounced boundary effect with a  $\approx$  58% increase in the small strain shear modulus in the square network as compared to rectangular (Fig. 12b), which is similar to a prior report [62]. Even in this network, the peak rate of increase of  $L_{\rm eff}$  corresponded to the onset of strain stiffening, and occurred at shear strains of 3.69% ( $\alpha$  = 0.18), 3.17% ( $\alpha$  = 0.14), and 2.70% ( $\alpha$  = 0.11) for prestrains of 0%, 0.5%, and 1%, respectively (Fig. 12c–g). Additionally, the small strain shear modulus was correlated to  $L_{\rm eff}$  for the different amounts prestress (Fig. 12h), similar to Fig. 9g. Therefore, the force chain-based predictions of the global mechanics also apply in the presence of boundary effects.

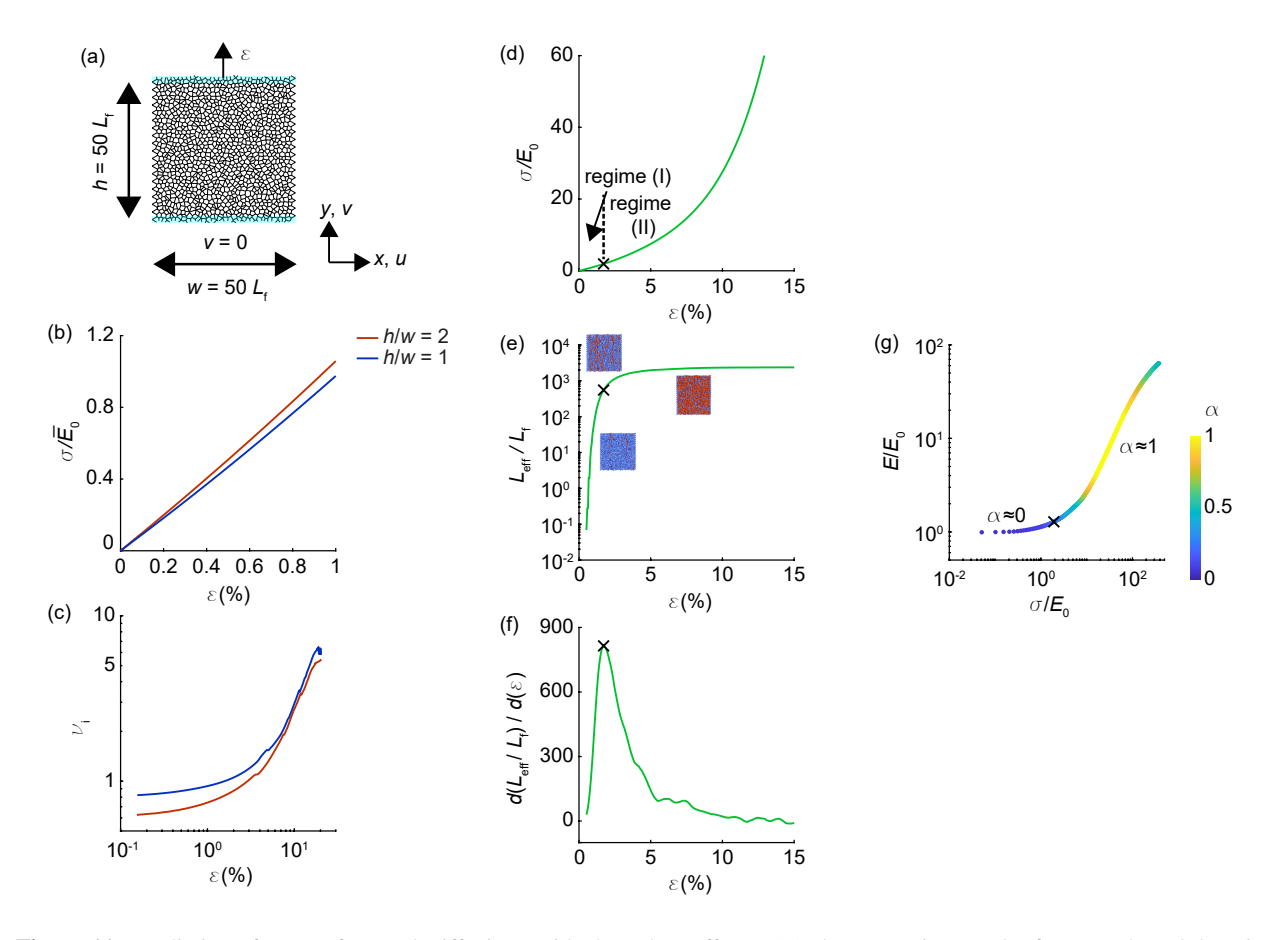


Figure 11: Prediction of onset of normal stiffening amidst boundary effects. (a) The Voronoi network of square-shaped domain (height-to-width ratio, h/w=1) subjected to uniaxial extension. The nodes at the bottom of the network were fixed, and the nodes at the top of the network were subjected to uniaxial extension  $\varepsilon$ . (b) Stress responses ( $\sigma$ ) at small strain,  $\varepsilon \in [0, 1\%]$ , were compared for both the square network (panel a) and the rectangular Voronoi network (h/w=2) described in the Results section. Stress was normalized by the small strain modulus of the rectangular network  $\overline{E}_0$ . (c) Incremental Poisson ratio ( $v_i$ ) as a function of  $\varepsilon$  for the square and rectangular network. (d) Stress-strain ( $\sigma$ - $\varepsilon$ ) curve for the square network. The stress axis was normalized by the small strain modulus ( $E_0$ ). (e) Evolution of the total length of force chains ( $L_{\rm eff}$ ) with  $\varepsilon$ . Insets show schematic diagrams of deformed networks with force chains shown in red. The force chain parameter  $L_{\rm eff}$  was normalized by the fiber length ( $L_f$ ). (f) Rate of evolution of force chains,  $dL_{\rm eff}/d\varepsilon$  plotted against the applied global strain  $\varepsilon$ . The rate was normalized by the fiber length ( $L_f$ ). The peak rate observed at  $\varepsilon=1.71\%$  (marked by "×") corresponds to the onset of strain stiffening and separates regimes I and II in the  $\sigma$ - $\varepsilon$  curve in panel d. The symbol "×" corresponds to the same strain in panels d, e, and f. (g) Tangent modulus (E) as a function of stress  $\sigma$  showing regimes I and II having exponents  $\alpha\approx0$  and  $\approx1$ , respectively. The axes were normalized by the small strain modulus  $E_0$ . The highest rate of evolution of force chains corresponds to a stiffening exponent  $\alpha=0.24$  (marked "×"). Panels d–g corresponded to the square network shown in panel a.

# References

- [1] Janmey, P. A., 1998, "The cytoskeleton and cell signaling: component localization and mechanical coupling," Physiol Rev, **78**(3), pp. 763–781.
- [2] Bausch, A. and Kroy, K., 2006, "A bottom-up approach to cell mechanics," Nat Phys, **2**(4), pp. 231–238.
- [3] Alberts, B., Johnson, A., Lewis, J., Raff, M., Roberts, K., and Walter, P., 2007, *Molecular Biology of the Cell*, Taylor & Francis Group, New York.

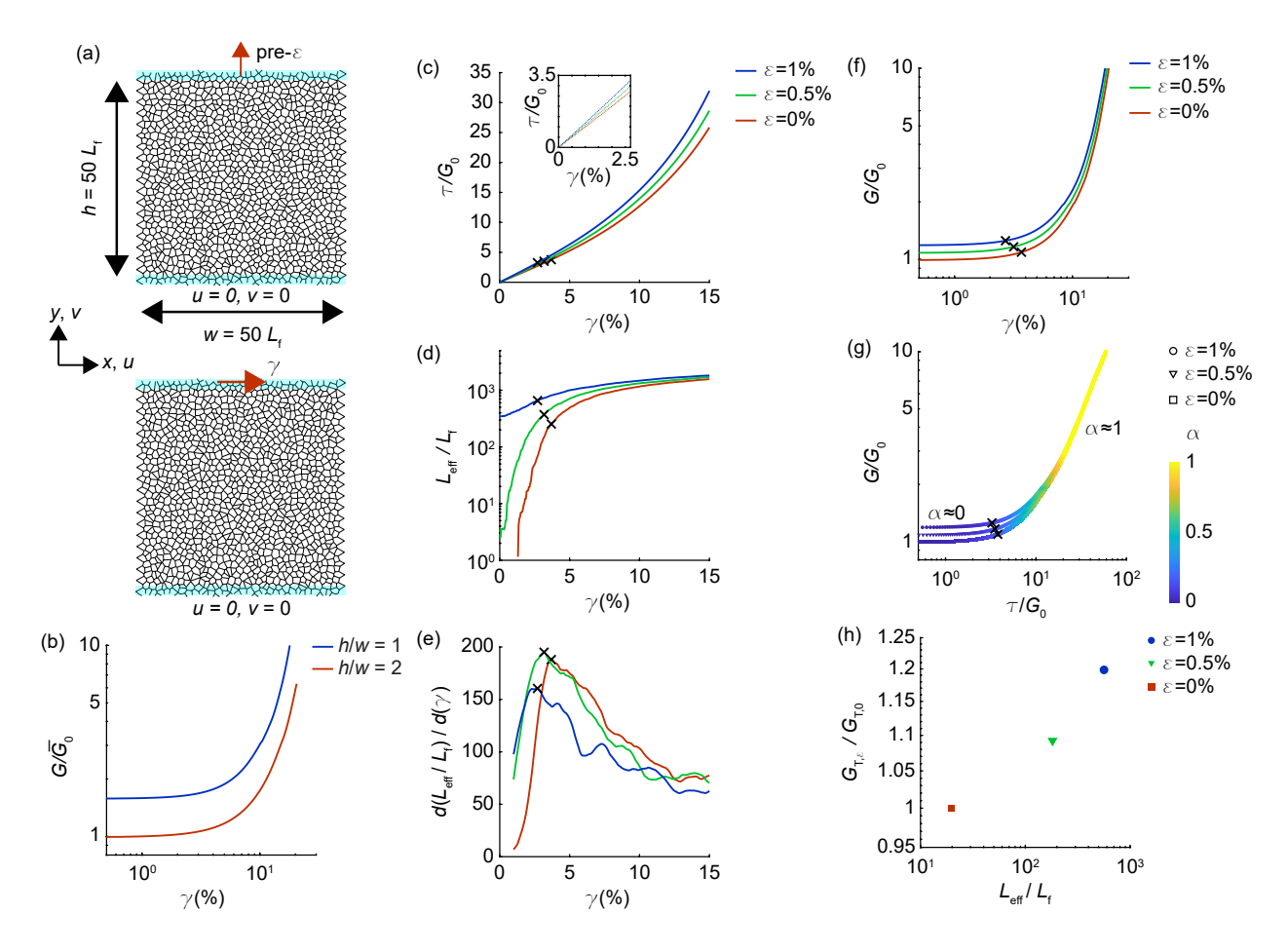


Figure 12: Prediction of onset of shear stiffening amidst boundary effects. (a) The prestressed square network described in Fig. 11 was subjected to shear. The nodes at the bottom of the network were fixed, and the nodes at the top of the network were subjected to uniaxial pretension ( $\varepsilon$ ) and shear ( $\gamma$ ). (b) Tangent shear modulus (G) of the square (panel a) and rectangular network (in main text) were compared during the shear deformation ( $\gamma$ ) at zero prestress. The modulus was normalized by the small strain shear modulus of the rectangular network at zero prestress  $\overline{G}_0$ . (c) Shear stress–strain ( $\tau$ – $\gamma$ ) plot of the square network at pretension  $\varepsilon = 0\%$ , 0.5% and 1%. The inset shows the stress responses at small shear strain,  $\gamma \in [0, 2.5\%]$ . The stress axis was normalized by the small strain shear modulus of the square network at zero prestress  $G_0$ . (d) Evolution of the normalized total length of force chains ( $L_{\rm eff}/L_{\rm f}$ ) with shear  $\gamma$  at pretension  $\varepsilon = 0\%$ , 0.5% and 1%. (e) Normalized rate of evolution of force chains ( $d(L_{\rm eff}/L_{\rm f})/d\gamma$ ) with shear at pretension  $\varepsilon = 0\%$ , 0.5% and 1%. The peak rates (marked "×") correspond to the onsets of strain stiffening at varying values of prestress. (f) Tangent shear modulus (G) as a function of  $\gamma$ . (g) Tangent shear modulus (G) as a function of stress  $\tau$  showing regime I having  $\alpha \approx 0$  and regime II having  $\alpha \approx 1$ . The stress was normalized by the small strain modulus of the network at zero prestress  $G_0$ . In panels f and g, the tangent modulus was also normalized by  $G_0$ . The onset points of stiffening as predicted in panel e are marked by "×" in panels c, d, f and g. (h) Tangent shear modulus at  $\gamma = 2\%$  at varying prestress ( $G_{T,\varepsilon}$ ) plotted against the normalized total length of force chains ( $L_{\rm eff}/L_{\rm f}$ ) in the respective deformed states.  $G_{T,\varepsilon}$  was normalized by the modulus corresponding to  $\varepsilon = 0$  (i.e.,  $G_{T,0}$ ). Panels c–h corresponded to the square network of panel a.

- [4] Laurens, N., Koolwijk, P. d., and De Maat, M., 2006, "Fibrin structure and wound healing," J Thromb Haemost, **4**(5), pp. 932–939.
- [5] Muiznieks, L. D. and Keeley, F. W., 2013, "Molecular assembly and mechanical properties of the extracellular matrix: A fibrous protein perspective," BBA-Mol Basis Dis, **1832**(7), pp. 866–875.
- [6] Kotlarchyk, M. A., Shreim, S. G., Alvarez-Elizondo, M. B., Estrada, L. C., Singh, R., Valdevit, L., Kniazeva, E., Gratton, E., Putnam, A. J., and Botvinick, E. L., 2011, "Concentration independent modulation of local micromechanics in a fibrin gel," Plos One, **6**(5), p. e20201.

- [7] Jones, C. A., Cibula, M., Feng, J., Krnacik, E. A., McIntyre, D. H., Levine, H., and Sun, B., 2015, "Micromechanics of cellularized biopolymer networks," P Natl Acad Sci USA, **112**(37), pp. E5117–E5122.
- [8] Shahsavari, A. and Picu, R., 2013, "Size effect on mechanical behavior of random fiber networks," Int J Solids Struct, **50**(20-21), pp. 3332–3338.
- [9] Proestaki, M., Ogren, A., Burkel, B., and Notbohm, J., 2019, "Modulus of fibrous collagen at the length scale of a cell," Exp Mech, **59**(9), pp. 1323–1334.
- [10] DiDonna, B. and Lubensky, T., 2005, "Nonaffine correlations in random elastic media," Phys Rev E, **72**(6), p. 066619.
- [11] Head, D., Levine, A., and MacKintosh, F., 2003, "Distinct regimes of elastic response and deformation modes of cross-linked cytoskeletal and semiflexible polymer networks," Phys Rev E, **68**(6), p. 061907.
- [12] Head, D., Levine, A., and MacKintosh, F., 2005, "Mechanical response of semiflexible networks to localized perturbations," Phys Rev E, **72**(6), p. 061914.
- [13] Chandran, P. L. and Barocas, V. H., 2006, "Affine versus non-affine fibril kinematics in collagen networks: theoretical studies of network behavior," J Biomech Eng—T ASME, **128**(2), pp. 259–270.
- [14] Hatami-Marbini, H. and Picu, R., 2008, "Scaling of nonaffine deformation in random semiflexible fiber networks," Phys Rev E, 77(6), p. 062103.
- [15] Liu, J., Koenderink, G., Kasza, K., MacKintosh, F., and Weitz, D., 2007, "Visualizing the strain field in semiflexible polymer networks: strain fluctuations and nonlinear rheology of F-actin gels," Phys Rev Lett, **98**(19), p. 198304.
- [16] Wen, Q., Basu, A., Winer, J. P., Yodh, A., and Janmey, P. A., 2007, "Local and global deformations in a strain-stiffening fibrin gel," New J Phys, **9**(11), p. 428.
- [17] Grimmer, P. and Notbohm, J., 2018, "Displacement propagation in fibrous networks due to local contraction," J Biomech Eng—T ASME, **140**(4), p. 041011.
- [18] Burkel, B., Proestaki, M., Tyznik, S., and Notbohm, J., 2018, "Heterogeneity and nonaffinity of cell-induced matrix displacements," Phys Rev E, **98**(5), p. 052410.
- [19] Licup, A. J., Münster, S., Sharma, A., Sheinman, M., Jawerth, L. M., Fabry, B., Weitz, D. A., and MacKintosh, F. C., 2015, "Stress controls the mechanics of collagen networks," P Natl Acad Sci USA, 112(31), pp. 9573–9578.
- [20] Vahabi, M., Sharma, A., Licup, A. J., Van Oosten, A. S., Galie, P. A., Janmey, P. A., and MacKintosh, F. C., 2016, "Elasticity of fibrous networks under uniaxial prestress," Soft matter, 12(22), pp. 5050–5060.
- [21] Picu, R., Deogekar, S., and Islam, M., 2018, "Poisson's contraction and fiber kinematics in tissue: insight from collagen network simulations," J Biomech Eng-T ASME, **140**(2), p. 021002.
- [22] Roeder, B. A., Kokini, K., Sturgis, J. E., Robinson, J. P., and Voytik-Harbin, S. L., 2002, "Tensile mechanical properties of three-dimensional type I collagen extracellular matrices with varied microstructure," J Biomech Eng-T ASME, **124**(2), pp. 214–222.

- [23] Janmey, P. A., McCormick, M. E., Rammensee, S., Leight, J. L., Georges, P. C., and MacKintosh, F. C., 2007, "Negative normal stress in semiflexible biopolymer gels," Nat Mater, 6(1), pp. 48–51.
- [24] Brown, A. E., Litvinov, R. I., Discher, D. E., Purohit, P. K., and Weisel, J. W., 2009, "Multiscale mechanics of fibrin polymer: gel stretching with protein unfolding and loss of water," Science, **325**(5941), pp. 741–744.
- [25] Vader, D., Kabla, A., Weitz, D., and Mahadevan, L., 2009, "Strain-induced alignment in collagen gels," Plos One, **4**(6), p. e5902.
- [26] Münster, S., Jawerth, L. M., Leslie, B. A., Weitz, J. I., Fabry, B., and Weitz, D. A., 2013, "Strain history dependence of the nonlinear stress response of fibrin and collagen networks," P Natl Acad Sci USA, **110**(30), pp. 12197–12202.
- [27] Kim, O. V., Litvinov, R. I., Weisel, J. W., and Alber, M. S., 2014, "Structural basis for the nonlinear mechanics of fibrin networks under compression," Biomaterials, **35**(25), pp. 6739–6749.
- [28] Sharma, A., Licup, A., Rens, R., Vahabi, M., Jansen, K., Koenderink, G., and MacKintosh, F., 2016, "Strain-driven criticality underlies nonlinear mechanics of fibrous networks," Phys Rev E, **94**(4), p. 042407.
- [29] Heussinger, C. and Frey, E., 2007, "Force distributions and force chains in random stiff fiber networks," Eur Phys J E, **24**(1), pp. 47–53.
- [30] Ronceray, P., Broedersz, C. P., and Lenz, M., 2016, "Fiber networks amplify active stress," P Natl Acad Sci USA, **113**(11), pp. 2827–2832.
- [31] Liang, L., Jones, C., Chen, S., Sun, B., and Jiao, Y., 2016, "Heterogeneous force network in 3D cellularized collagen networks," Phys Biol, **13**(6), p. 066001.
- [32] Mann, A., Sopher, R. S., Goren, S., Shelah, O., Tchaicheeyan, O., and Lesman, A., 2019, "Force chains in cell–cell mechanical communication," J R Soc Interface, **16**(159), p. 20190348.
- [33] Ruiz-Franco, J. and van Der Gucht, J., 2022, "Force Transmission in Disordered Fibre Networks," Front. Cell Dev. Biol., **10**, p. 931776.
- [34] Majmudar, T. S. and Behringer, R. P., 2005, "Contact force measurements and stress-induced anisotropy in granular materials," Nature, **435**(7045), pp. 1079–1082.
- [35] Duran, J., 1997, Sands, powders, and grains: An introduction to the physics of granular materials, Eyrolles, France.
- [36] Cates, M., Wittmer, J., Bouchaud, J.-P., and Claudin, P., 1998, "Jamming, force chains, and fragile matter," Phys Rev Lett, **81**(9), p. 1841.
- [37] Blair, D. L., Mueggenburg, N. W., Marshall, A. H., Jaeger, H. M., and Nagel, S. R., 2001, "Force distributions in three-dimensional granular assemblies: Effects of packing order and interparticle friction," Phys Rev E, **63**(4), p. 041304.
- [38] Rosakis, P., Notbohm, J., and Ravichandran, G., 2015, "A model for compression-weakening materials and the elastic fields due to contractile cells," J Mech Phys Solids, **85**, pp. 16–32.
- [39] Lindström, S. B., Vader, D. A., Kulachenko, A., and Weitz, D. A., 2010, "Biopolymer network geometries: Characterization, regeneration, and elastic properties," Phys Rev E, **82**(5), p. 051905.

- [40] Arzash, S., Shivers, J. L., Licup, A. J., Sharma, A., and MacKintosh, F. C., 2019, "Stress-stabilized subisostatic fiber networks in a ropelike limit," Phys Rev E, **99**(4), p. 042412.
- [41] Maxwell, J. C., 1864, "L. on the calculation of the equilibrium and stiffness of frames," Lond Edinb Dublin Philos Mag J Sci, **27**(182), pp. 294–299.
- [42] Lake, S. P., Hadi, M. F., Lai, V. K., and Barocas, V. H., 2012, "Mechanics of a fiber network within a non-fibrillar matrix: model and comparison with collagen-agarose co-gels," Ann Biomed Eng, **40**(10), pp. 2111–2121.
- [43] Nachtrab, S., Kapfer, S. C., Arns, C. H., Madadi, M., Mecke, K., and Schröder-Turk, G. E., 2011, "Morphology and Linear-Elastic Moduli of Random Network Solids," Adv Mater, **23**(22-23), pp. 2633–2637.
- [44] Heussinger, C. and Frey, E., 2006, "Stiff polymers, foams, and fiber networks," Phys Rev Lett, **96**(1), p. 017802.
- [45] Kumar, S. and Kurtz, S. K., 1993, "Properties of a two-dimensional Poisson-Voronoi tesselation: a Monte-Carlo study," Mater Charact, **31**(1), pp. 55–68.
- [46] Cavalcante, F. S., Ito, S., Brewer, K., Sakai, H., Alencar, A. M., Almeida, M. P., Andrade Jr, J. S., Majumdar, A., Ingenito, E. P., and Suki, B., 2005, "Mechanical interactions between collagen and proteoglycans: implications for the stability of lung tissue," J Appl Physiol, **98**(2), pp. 672–679.
- [47] Knudsen, L. and Ochs, M., 2018, "The micromechanics of lung alveoli: structure and function of surfactant and tissue components," Histochem Cell Biol, **150**(6), pp. 661–676.
- [48] Hatami-Marbini, H. and Rohanifar, M., 2021, "Nonlinear mechanical properties of prestressed branched fibrous networks," Biophys J, **120**(3), pp. 527–538.
- [49] Picu, R., 2011, "Mechanics of random fiber networks—a review," Soft Matter, 7(15), pp. 6768–6785.
- [50] Shahsavari, A. and Picu, R., 2012, "Model selection for athermal cross-linked fiber networks," Phys Rev E, **86**(1), p. 011923.
- [51] Tyznik, S. and Notbohm, J., 2019, "Length scale dependent elasticity in random three-dimensional fiber networks," Mech Mater, 138, p. 103155.
- [52] Head, D. A., Levine, A. J., and MacKintosh, F., 2003, "Deformation of cross-linked semiflexible polymer networks," Phys Rev Lett, **91**(10), p. 108102.
- [53] Wilhelm, J. and Frey, E., 2003, "Elasticity of stiff polymer networks," Phys Rev Lett, **91**(10), p. 108103.
- [54] Feng, J., Levine, H., Mao, X., and Sander, L. M., 2015, "Alignment and nonlinear elasticity in biopolymer gels," Phys Rev E, **91**(4), p. 042710.
- [55] Van Oosten, A. S., Vahabi, M., Licup, A. J., Sharma, A., Galie, P. A., MacKintosh, F. C., and Janmey, P. A., 2016, "Uncoupling shear and uniaxial elastic moduli of semiflexible biopolymer networks: compression-softening and stretch-stiffening," Sci Rep, 6, p. 19270.
- [56] Proestaki, M., Burkel, B., Galles, E. E., Ponik, S. M., and Notbohm, J., 2021, "Effect of matrix heterogeneity on cell mechanosensing," Soft Matter, 17, pp. 10263–10273.

- [57] Sarkar, M. and Notbohm, J., 2022, "Quantification of Errors in Applying DIC to Fiber Networks Imaged by Confocal Microscopy," Exp Mech.
- [58] Natário, P., Silvestre, N., and Camotim, D., 2014, "Web crippling failure using quasi-static FE models," Thin Wall Struct, **84**, pp. 34–49.
- [59] Islam, M. and Picu, R., 2018, "Effect of network architecture on the mechanical behavior of random fiber networks," J Appl Mech, **85**(8), p. 081011.
- [60] Peters, J., Muthuswamy, M., Wibowo, J., and Tordesillas, A., 2005, "Characterization of force chains in granular material," Phys Rev E, **72**(4), p. 041307.
- [61] Licup, A. J., Sharma, A., and MacKintosh, F. C., 2016, "Elastic regimes of subisostatic athermal fiber networks," Phys Rev E, **93**(1), p. 012407.
- [62] Merson, J. and Picu, R., 2020, "Size effects in random fiber networks controlled by the use of generalized boundary conditions," Int J Solids Struct, **206**, pp. 314–321.
- [63] Jen, C. J. and McIntire, L. V., 1982, "The structural properties and contractile force of a clot," Cell Motil Cytoskel, **2**(5), pp. 445–455.
- [64] Taylor, C. A. and Humphrey, J., 2009, "Open problems in computational vascular biomechanics: hemodynamics and arterial wall mechanics," Comput Method Appl M, **198**(45-46), pp. 3514–3523.
- [65] Ingber, D. E., 2006, "Cellular mechanotransduction: putting all the pieces together again," FASEB J, **20**(7), pp. 811–827.
- [66] Destrade, M., Liu, Y., Murphy, J. G., and Kassab, G. S., 2012, "Uniform transmural strain in prestressed arteries occurs at physiological pressure," J Theor Biol, **303**, pp. 93–97.
- [67] Luo, J., Li, S., Xu, J., Chai, M., Gao, L., Yang, C., and Shi, X., 2021, "Biomimetic Strain-Stiffening Hydrogel with Crimped Structure," Adv Funct Mater, **31**(43), p. 2104139.
- [68] Chen, W., Kumari, J., Yuan, H., Yang, F., and Kouwer, P. H., 2022, "Towards Tissue-like Material Properties: Inducing In Situ Adaptive Behavior in Fibrous Hydrogels," Adv Mater, p. e2202057.
- [69] Islam, M. and Picu, R., 2019, "Random fiber networks with inclusions: The mechanism of reinforcement," Phys Rev E, **99**(6), p. 063001.
- [70] Ban, E., Wang, H., Franklin, J. M., Liphardt, J. T., Janmey, P. A., and Shenoy, V. B., 2019, "Strong triaxial coupling and anomalous Poisson effect in collagen networks," P Natl Acad Sci USA, **116**(14), pp. 6790–6799.